Article

Spectroscopic and Computational Studies of the de Novo Designed Protein DF2t: Correlation to the Biferrous Active Site of Ribonucleotide Reductase and Factors That Affect O Reactivity

Pin-pin Wei, Andrew J. Skulan, Herschel Wade, William F. DeGrado, and Edward I. Solomon

J. Am. Chem. Soc., **2005**, 127 (46), 16098-16106• DOI: 10.1021/ja053661a • Publication Date (Web): 27 October 2005

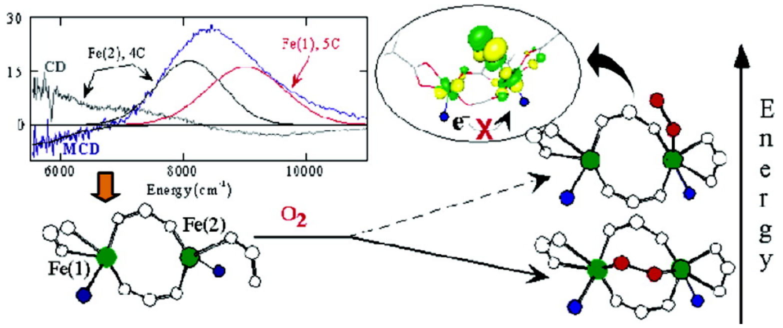

Journal of the American Chemical Society is published by the American Chemical Society. 1155 Sixteenth Street N.W., Washington, DC 20036

J|A|C|S
ARTICLES
Published on Web 10/27/2005

Spectroscopic and Computational Studies of the de Novo Designed Protein DF2t: Correlation to the Biferrous Active Site of Ribonucleotide Reductase and Factors That Affect O_2 Reactivity

Pin-pin Wei,[†] Andrew J. Skulan,[†] Herschel Wade,[‡] William F. DeGrado,*[,‡] and
Edward I. Solomon*[,†]

Contribution from the Department of Chemistry, Stanford University, Stanford, California 94305, and Department of Biochemistry and Biophysics, School of Medicine, University of Pennsylvania, Philadelphia, Pennsylvania 19104-6059

Received June 3, 2005; E-mail: wdegrado@mail.med.upenn.edu; edward.solomon@stanford.edu

Abstract: DF2t, a de novo designed protein that mimicks the active-site structure of many non-heme biferrous enzymes, has been studied using a combination of circular dichroism (CD), magnetic circular dichroism (MCD), and variable-temperature variable-field (VTVH) MCD. The active site of DF2t is found to have one five-coordinate iron and one four-coordinate iron, which are weakly antiferromagnetically coupled through a μ-1,3 carboxylate bridge. These results bear a strong resemblance to the spectra of *Escherichia coli* ribonucleotide reductase (R2), and density functional theory calculations were conducted on the W48F/D84E R2 mutant in order to determine the energetics of formation of a monodentate end-on-bound O_2 to one iron in the binuclear site. The μ-1,3 carboxylate bridges found in O_2-activating enzymes lack efficient superexchange pathways for the second electron transfer (i.e., the OH/oxo bridge in hemerythrin), and simulations of the binding of O_2 in a monodentate end-on manner revealed that the bridging carboxylate ligands do not appear capable of transferring an electron to O_2 from the remote Fe. Comparison of the results from previous studies of the μ-1,2 biferric-peroxo structure, which bridges both irons, finds that the end-on superoxide mixed-valent species is considerably higher in energy than the bridging peroxo-diferric species. Thus, one of the differences between O_2-activating and O_2-binding proteins appears to be the ability of O_2 to bridge both Fe centers to generate a peroxo intermediate capable of further reactivity.

Introduction

The use of models to mimic active sites has been an effective approach in bioinorganic chemistry.[1−6] However, the hydrophobic active-site environments, the three-dimensional arrangement of the primary ligands, and the influence of the second-shell amino acids on the reactivity of many enzyme-bound cofactors are often difficult to duplicate.[7] This is evident in the case of non-heme binuclear iron sites in enzymes such as methane monooxygenase (MMOH),[5,8−10] ribonucleotide reductase (R2),[11−13] and Δ^9-desaturase (Δ^9D).[4,14,15] In these three proteins, remarkably similar core ligands give rise to variations in the geometry of the resting state which contribute to their differences in O_2 reactivity.

The combined use of molecular biology and spectroscopy to study the active sites of enzymes has improved our understanding of electron pathways and the requirements for oxygen activation. However, it is often difficult to unravel the effects of individual changes within an extensive protein structure.[16] De novo proteins that can mimic the effects of first- and second-sphere interactions on structure and reactivity are now emerging.[17,18] This is significant since amino acids in the second shell

---

[†] Stanford University.

[‡] University of Pennsylvania.

(1) Dong, Y. H.; Zang, Y.; Shu, L. J.; Wilkinson, E. C.; Que, L.; Kauffmann, K.; Münck, E. *J. Am. Chem. Soc.* **1997**, *119*, 12683−12684.
(2) Costas, M.; Mehn, M. P.; Jensen, M. P.; Que, L., Jr. *Chem. Rev.* **2004**, *104*, 939−986.
(3) Tshuva, E. Y.; Lippard, S. J. *Chem. Rev.* **2004**, *104*, 987−1012.
(4) Solomon, E. I.; Brunold, T. C.; Davis, M. I.; Kemsley, J. N.; Lee, S. K.; Lehnert, N.; Neese, F.; Skulan, A. J.; Yang, Y. S.; Zhou, J. *Chem. Rev.* **2000**, *100*, 235−349.
(5) Wallar, B. J.; Lipscomb, J. D. *Chem. Rev.* **1996**, *96*, 2625−2658.
(6) Reedy, C. J.; Gibney, B. R. *Chem. Rev.* **2004**, *104*, 617−649.
(7) Lu, Y.; Berry, S. M.; Pfister, T. D. *Chem. Rev.* **2001**, *101*, 3047−3080.
(8) Rosenzweig, A. C.; Nordlund, P.; Takahara, P. M.; Frederick, C. A.; Lippard, S. J. *Chem. Biol.* **1995**, *2*, 409−418.
(9) Merkx, M.; Kopp, D.; Sazinsky, M.; Blazyk, J.; Muller, J.; Lippard, S. J. *Angew. Chem., Int. Ed.* **2001**, *40*, 2782−2807.
(10) Baik, M. H.; Newcomb, M.; Friesner, R. A.; Lippard, S. J. *Chem. Rev.* **2003**, *103*, 2385−2420.
(11) Nordlund, P.; Eklund, H. *J. Mol. Biol.* **1993**, *232*, 123−164.
(12) Yang, Y. S.; Baldwin, J.; Ley, B. A.; Bollinger, J. M., Jr.; Solomon, E. I. *J. Am. Chem. Soc.* **2000**, *122*, 8495−8510.
(13) Stubbe, J.; Nocera, D. G.; Yee, C. S.; Chang, M. C. *Chem. Rev.* **2003**, *103*, 2167−2202.
(14) Yang, Y. S.; Broadwater, J. A.; Pulver, S. C.; Fox, B. G.; Solomon, E. I. *J. Am. Chem. Soc.* **1999**, *121*, 2770−2783.
(15) Shanklin, J.; Cahoon, E. B. *Annu. Rev. Plant Physiol. Plant Mol. Biol.* **1998**, *49*, 611−641.
(16) Wei, P. P.; Skulan, A. J.; Mitic, N.; Yang, Y. S.; Saleh, L.; Bollinger, J. M.; Solomon, E. I. *J. Am. Chem. Soc.* **2004**, *126*, 3777−3788.
(17) Papoian, G. A.; DeGrado, W. F.; Klein, M. L. *J. Am. Chem. Soc.* **2003**, *125*, 560−569.
(18) Magistrato, A.; DeGrado, W. F.; Laio, A.; Rothlisberger, U.; VandeVondele, J.; Klein, M. L. *J. Phys. Chem. B.* **2003**, *107*, 4182−4188.

10.1021/ja053661a CCC: $30.25

maintain the structure of metal binding sites, which can tune their reactivity and/or substrate access to the active-site pocket.[19]

Recent advances using computational methods confirmed by experiment have led to the design of self-assembling heterotetrameric and homo-dimeric four-helix bundles named the "due ferro" (DF) family.[20] The DF scaffold approximates the four-helix bundles of natural diiron proteins, and the core ligand set provided by the DF design matches those of the binuclear non-heme iron enzymes with two bridging carboxylates from glutamate (Glu), and each metal terminally ligated with a histidine (His) and a Glu. The di-zinc form of DF1 and the di-Mn(II) form of single-site mutants of this protein have been crystallographically characterized.[20,21] As is the case for natural diiron proteins, there is variation in the dimetal sites in these designed structures; even individual dimers in the asymmetric unit show differences in exogenous bridging solvent molecules as well as more subtle carboxylate shifts.[22,23] Overall, the active-site geometry shows the strongest similarity to bimanganous and biferrous forms of ribonucleotide reductase,[11,24,25] ruberythrin,[26] and Δ^9-desaturase.[20] More recently, a more soluble version of DF1 was engineered (designated DF2t) by increasing the polarity of the solvent-accessible side chains[27] and optimizing the "turn" between the two helices.[28] In general, the structures of biferrous (unpublished) and di-Zn(II) DF2t[28] active sites are within the range of structures observed for derivatives of DF1. However, past experience with DF1 and other diiron proteins indicates that the geometries observed will vary with the crystallization conditions, and it is important to fully characterize the geometry and reactivity of the reduced state in solution.

The application of spectroscopic techniques to the biferrous site in DF2t and future mutants allows the possibility of systematically exploring the influence of the solvent-accessibility and the first- and second-sphere amino acids on the biferrous center. This, along with the library of well-characterized naturally occurring diiron enzymes, can provide insight into factors which affect the structure and reactivity of a biferrous center. The functional diversity of these biferrous non-heme enzymes is apparent in their dioxygen reactivity (desaturation, hydroxylation, and radical formation). It is thus of interest to fully characterize the geometric and electronic structural properties of the biferrous site of this de novo protein, in order to explore the restraints imposed on the active-site structure by the bonding derived from the four-helix bundle tertiary protein structure and its effects on O_2 reactivity.

This study utilizes a combination of circular dichroism (CD), magnetic circular dichroism (MCD), and variable-temperature variable-field (VTVH) MCD spectroscopic techniques to obtain insight into the geometric and electronic structure of the binuclear ferrous center of DF2t. It is further supported by density functional calculations exploring the site geometry related to O_2 reactivity in a biferrous active site. The computational model used is *Escherichia coli* R2-D84E, as the crystal structure of biferrous DF2t was unavailable. While previous DF family crystal structures seemed to resemble Δ^9D, the spectroscopy presented below indicates that DF2t is in fact very similar to R2 and its D84E variant. In addition to having a well-defined crystal structure, R2-D84E reacts with O_2 to form a peroxy intermediate which has been spectroscopically characterized as a cis-μ-1,2 peroxo-diferric site.[29] DF2t also shows a fast reaction with O_2, although the peroxo-diferric intermediate has not been observed (vide infra). Therefore, the well-characterized resting structure of R2-D84E was used in calculations which evaluate the requirements for oxygen activation.

Experimental Section

A. Sample Preparation. MOPS buffer (Sigma), sodium chloride (Sigma), ferrous ammonium sulfate hexahydrate (Mallinckrodt), deuterium oxide (99.9 atom % D, Aldrich), sodium dithionite (Sigma), and glycerol (98% D, Cambridge Isotope Laboratories) were commercially purchased and used as obtained. Deuterated buffer was degassed with 99.9% pure argon; glycerol was degassed by heating under vacuum overnight and then finished with 10 freeze−pump−thaw cycles at 10^{-3} Torr. Protein samples were rapidly degassed by purging with 10 cycles of vacuum/argon. The protein was reduced using methyl viologen and dithionite in deuterated buffer, and the final pH was 7.0. The protein samples were prepared and loaded into the sample holders in an inert atmosphere.

DF2t was expressed and purified as previously reported.[20] The protein concentration was determined by using the molar extinction coefficient at 280 nm (9600 M^{-1} cm^{-1} per DF2t monomer in the apo state). Buffer exchange was carried out by adding deuterated buffer to the sample and concentrating the sample to 2−3 mM. This process was repeated until the percentage of D_2O was greater than 99.9% of the solvent.

The procedure for Fe(II)-loading into the apo protein under anaerobic conditions can be found in ref 16. The degassed iron(III)-loaded protein was fully reduced with 1 μL of 5 mM methyl viologen and 10 μL of 10 mM dithionite for CD. Protein samples were prepared for MCD in the same way as for CD, with an additional step of mixing the protein with 60% (v/v) glycerol-d_6 until homogeneous to create a suitable glass. From CD studies, the glycerol was found to have no effect on the biferrous site. The samples were then immediately frozen in liquid nitrogen.

B. CD and MCD Spectroscopy. CD studies were performed on a JASCO J200D spectropolarimeter operating with a liquid nitrogen-cooled InSb detector in the 560−2000 nm region. Low-temperature MCD and VTVH data were acquired on this spectropolarimeter, modified to accommodate an Oxford Instruments SM4000 7-T superconducting magnet capable of magnetic fields up to 7.0 T and temperatures down to 1.6 K. Protein samples prepared for MCD studies were slowly inserted into the cryostat to reduce strain in the resulting optical glass.

The CD and MCD spectra were fit using a constrained nonlinear least-squares procedure in order to find the minimum number of ligand field transitions required to simultaneously fit both spectra. Each spectroscopic method has a different selection rule; thus, transitions can have different intensities and signs but similar energies. The transition energies and amplitude obtained are used for elucidating the geometric and electronic structures of the binuclear Fe(II) active sites.

---

(19) Maglio, O.; Nastri, F.; Pavone, V.; Lombardi, A.; DeGrado, W. F. *Proc. Natl. Acad. Sci. U.S.A.* **2003**, *100*, 3772−3777.

(20) Di Costanzo, L.; Wade, H.; Geremia, S.; Randaccio, L.; Pavone, V.; DeGrado, W. F.; Lombardi, A. *J. Am. Chem. Soc.* **2001**, *123*, 12749−12757.

(21) Lombardi, A.; Summa, C.; DeGrado, W. F. *Proc. Natl. Acad. Sci.* **2000**, *97*, 6298−6305.

(22) Yoon, S.; Lippard, S. J. *J. Am. Chem. Soc.* **2004**, *126*, 16692−16693.

(23) DeGrado, W. F.; Di Costanzo, L.; Geremia, S.; Lombardi, A.; Pavone, V.; Randaccio, L. *Angew. Chem., Int. Ed.* **2003**, *42*, 417−420.

(24) Logan, D.; Su, X.; Aberg, A.; Regnstrom, K.; Hajdu, J.; Eklund, H.; Nordlund, P. *Structure* **1996**, *4*, 1053−1064.

(25) Voegtli, W. C.; Sommerhalter, M.; Saleh, L.; Baldwin, J.; Bollinger, J. M.; Rosenzweig, A. C. *J. Am. Chem. Soc.* **2003**, *125*, 15822−15830.

(26) deMare, F.; Kurtz, D. M. J.; Nordlund, P. *Nat. Struct. Biol.* **1996**, *3*, 539−546.

(27) Pasternak, A.; Kaplan, J.; DeGrado, W. F. *Protein Sci.* **2001**, *10*, 958−969.

(28) Lahr, S. J.; Engel, D. E.; Stayrook, S. E.; Maglio, O.; North, B.; Geremia, S.; Lombardi, A.; DeGrado, W. F. *J. Mol. Biol.* **2005**, *346*, 1441−1454.

(29) Skulan, A. J.; Brunold, T. C.; Baldwin, J.; Saleh, L.; Bollinger, J. M.; Solomon, E. I. *J. Am. Chem. Soc.* **2004**, *126*, 8842−8855.

VTVH MCD data (MCD intensity, temperature, and applied magnetic field) were fit with a series of non-Kramers doublets using a simplex routine that minimizes the χ^2 value. A goodness-of-fit parameter (χ^2/number of float parameters) was utilized in the comparison of different fit results. The $g_{||}$ values of the ground and excited sublevels as well as the energies obtained give information concerning the spin states and bridging of the dimer. In addition, a spin-projection model was applied to confirm the results obtained from the doublet model and to identify the specific Fe center of the dimer associated with the ligand field transition being studied by VTVH MCD. This procedure is described in the Results section.

C. Density Functional Calculations. Density functional theory (DFT) calculations were carried out on an SGI 2000 computer using the Jaguar 4.1 package for geometry optimizations of the models described below. All calculations were spin-unrestricted, broken symmetry, allowing for an accurate spin-polarized description of the electronic structure of antiferromagnetically coupled systems. The density functional was BP86. For geometry optimizations, the iron atoms were described by the LACVP* double-ζ basis set,[30] atoms within three bonds of the iron atoms used 6-31G*, and all others used 6-31G. The basis set size was increased to triple-ζ for determining energies, using the LACV3P* basis set.[31,32] To quantitatively calculate factors which affect the O_2 reactivity of the binuclear ferrous site, we build on the results of our past studies on the diiron active site (R2),[29,33] which is structurally well-defined and has strong spectral similarities to DF2t (vide infra).

Results

A. CD and Low-Temperature MCD Spectroscopy. Near-IR CD and MCD spectra for reduced DF2t are shown in Figure 1, with the Gaussian fit of the data shown in blue. The CD spectrum (Figure 1A) is comprised of three transitions at 5300, 7900, and 8900 cm^{-1}. The MCD spectrum (Figure 1B) shows a small negative peak at 5450 cm^{-1} and an asymmetrical peak near 8500 cm^{-1} that can be resolved into two bands at 8090 and 9015 cm^{-1}. The MCD spectra were taken at 1.6 K; thus, they have sharper bandwidths, and the band energies shift slightly relative to the CD data taken at 278 K. No further transitions are visible up to the protein absorbance at 280 nm. The CD and MCD spectra of DF2t prepared by loading Fe(II) into the apo protein and by chemically reducing the Fe_2(III) form overlay within standard deviation.

The MCD of aqueous Fe(II) overlaid with DF2t clearly shows no overlap, indicating that unbound Fe(II) is not contributing to the spectrum of DF2t (Supporting Information A). The three peaks of DF2t reflect two inequivalently bound Fe(II), as a single ferrous ion can only give rise to two peaks in the near-IR region. The two peaks above 8000 cm^{-1} in DF2t are separated by less than 1000 cm^{-1}, eliminating the possibility of a six-coordinate iron. A transition at greater than 8000 cm^{-1} (which is not associated with six-coordinate Fe^{II}) requires that at least one iron be five-coordinate (5C). The presence of the transition at 5450 cm^{-1}, along with the absence of a transition at >10 000 cm^{-1}, indicates that there is also one four-coordinate (4C) iron present. Thus, from the ligand field transitions present in the above CD/MCD spectra, it can be deduced that DF2t is composed of one five-coordinate iron and one four-coordinate iron (5C,4C).[34]

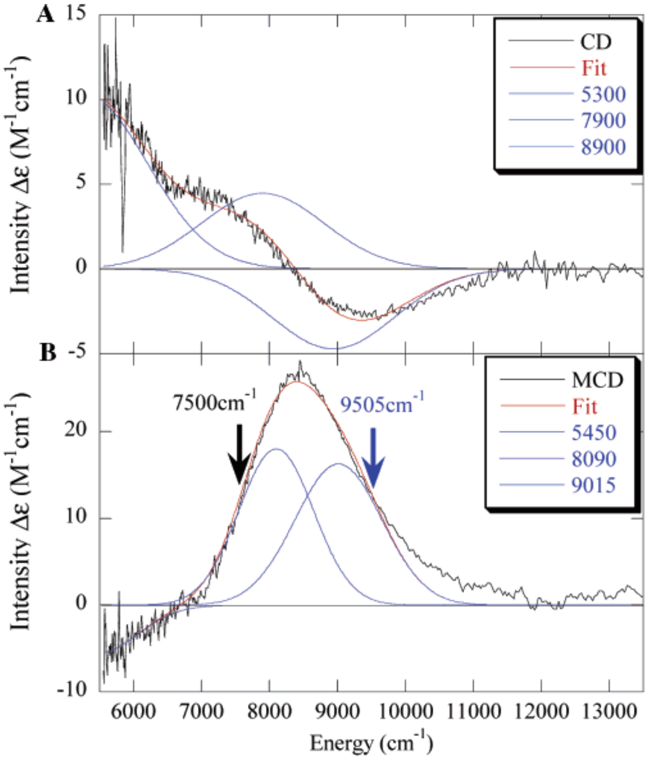

Figure 1. (A) CD spectrum of DF2t, recorded at 5 °C, and (B) MCD spectrum of DF2t, recorded at 1.6 K and 7 T. The experimental data (black line) are fit to the individual Gaussian band shapes (blue line). The arrows mark where the VTVH MCD data were collected.

B. VTVH MCD Spectroscopy. The MCD intensity of reduced DF2t increases as temperature decreases, indicating that these transitions are MCD *C*-terms associated with paramagnetic doublets that are split by a magnetic field. The field saturation curves at 7500 and 9500 cm^{-1} on the composite MCD peak (Figure 1B, blue and black arrows) are shown in Figure 2. These energies were chosen in order to minimize contributions from the adjacent, overlapping band. Both VTVH curves are nested, with the high-temperature data offset from the low-temperature data when the isotherms are plotted as a function of $\beta H/2kT$. This is characteristic of rhombic zero-field splitting (ZFS) of a non-Kramers doublet ground state and arises from temperature-dependent nonlinear field-induced mixing between the sublevels of the doublet. The VTVH data are similar but do not overlay within standard deviation for the two bands. Due to the low peak intensity, satisfactory VTVH data could not be collected at ~5500 cm^{-1}. Analysis of these VTVH and MCD data taken at 7500 and 9500 cm^{-1} provides the ground state of the Fe_2^{II} center, which gives further insight into the Fe coordination and nature of the bridging ligands.

---

(30) Hay, P.; Wadt, W. *J. Chem. Phys.* **1985**, *82*, 299−310.

(31) The residue truncation was performed as follows: the α-carbon was replaced by a hydrogen atom with concomitant shortening of the α-C−β-C bond to 1.08 Å, with the β-C retaining its original position. This hydrogen was then frozen in all geometry optimizations.

(32) The hydrogen-bonding residues were truncated to the smallest reasonable models, providing hydrogen-bonding interactions similar to those observed in the protein. These were Q43, formamide, $COHNH_2$; Q87, ammonia, NH_3; W111, ammonia, NH_3; S114, water, H_2O; Y122, water, H_2O; D237, formate, CHO_2^-. The positions of the heavy atoms (C, N, O) were frozen along with the positions of hydrogens replacing carbon atoms. Q43 and Q87 were modeled differently (as formamide and ammonia, respectively), as the R-group nitrogen of Q43 was located 2.8 Å from a carboxylate oxygen on D237, suggesting hydrogen bonding between these two residues which may have been of importance to the geometry of the active site. W/F48 residue, the second mutation from *E. coli* R2, was not included in the model as it does not coordinate to either iron or iron-coordinated residues.

(33) Moënne-Loccoz, P.; Baldwin, J.; Ley, B. A.; Loehr, T. M.; Bollinger, J. M. *Biochemistry* **1998**, *37*, 14659−14663.

(34) Solomon, E. I.; Pavel, E. G.; Loeb, K. E.; Campochiaro, C. *Coord. Chem. Rev.* **1995**, *144*, 369−460.

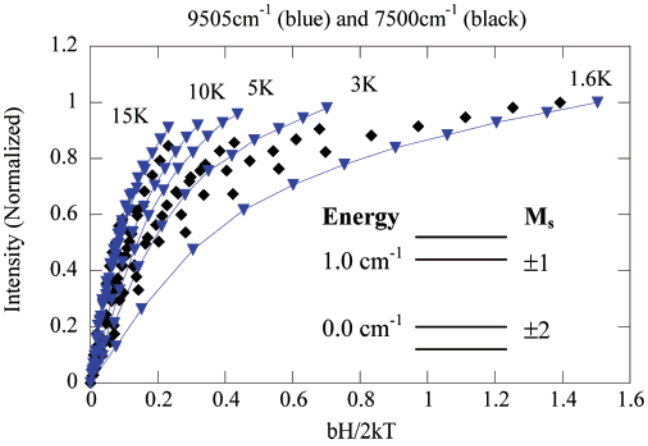

Figure 2. VTVH MCD of DF2t at 9505 (blue) and 7500 cm^{-1} (black). 2 K, 7 K, 20 K, and 25 K saturation curves were removed for clarity.

The VTVH MCD data were fit using the MCD intensity expression for a non-Kramers system, allowing for the effects of a linear *B*-term from field-induced mixing between states and the presence of excited sublevels of the ground state, as given by eq 1:[34−37]

$$\Delta\epsilon = \sum_i \left[(A_{\mathrm{sat\ lim}})_i \left(\int_0^{\pi/2} \frac{\cos^2\theta \sin\theta}{\Gamma_i} g_{\|i}\beta H \alpha_i \, d\theta - \sqrt{2}\frac{M_z}{M_{xy}} \int_0^{\pi/2} \frac{\sin^3\theta}{\Gamma_i} g_{\perp i}\beta H \alpha_i \, d\theta \right) + B_i H \gamma_i \right] \quad (1)$$

where

$$\Gamma_i = \sqrt{\delta_i^{\,2} + (g_{\|i}\beta H\cos\theta)^2 + (g_{\perp i}\beta H \sin\theta)^2}$$

$$\alpha_i = \frac{e^{-(E_i - \Gamma_i/2)/kT} - e^{-(E_i + \Gamma_i/2)/kT}}{\sum_j e^{-(E_j - \Gamma_j/2)/kT} + e^{-(E_j + \Gamma_j/2)/kT}}$$

$$\gamma_i = \frac{e^{-(E_i - \delta_i/2)/kT} + e^{-(E_i + \delta_i/2)/kT}}{\sum_j e^{-(E_j - \beta_j/2)/kT} + e^{-(E_j + \delta_j/2)/kT}}$$

$(A_{\mathrm{sat\ lim}})_i$, B_i, δ_i, $g_{\|i}$, and $g_{\perp i}$ are the *C*-term and *B*-term MCD intensities, the rhombic ZFS, and the dimer *g* values of the *i*th doublet, respectively. E_i is the energy of the *i*th sublevel, and the energy of the ground state is defined as zero. The Boltzmann population over all states has been included in both the *C*-term and the *B*-term intensities as the factors α_i and γ_i, respectively. *H* is the applied magnetic field, *k* is the Boltzmann constant, and M_z and M_{xy} are the transition dipole moments for the directions indicated.

Table 1. VTVH MCD Fit Parameters of DF2t, Δ^9D (Ref 14), and *E. coli* R2 (Ref 38)

	DF2t		Δ^9D	*E. coli* R2
	7500 cm^{-1}	9500 cm^{-1}	7700 cm^{-1}	7700 cm^{-1}
δ_1	0.3	0.3	0	4.6
$g_\|$ (ground)	8	8	0	8
δ_2	1.1	1.2	2	4.6
$g_\|$ (excited)	4	4	16	4
E (cm^{-1})	1.9	1.9	10.57	6
J (cm^{-1})	−0.8	−0.8	$<\sim -1.0$	−0.44
D_1 (cm^{-1})	10	10	$-15 < D < -5$	−10
D_2 (cm^{-1})	−5	−5	$-15 < D < -5$	4

The lowest-temperature (1.6 K) data collected at 7500 cm^{-1} for DF2t (black diamonds in Figure 2) were fit using eq 1 by floating the $A_{\mathrm{sat\ lim}}$, *B*, δ, and $g_\|$, while fixing $g_\perp$ and the polarization ratio M_z/M_{xy} at zero. The best fit to the complete data set requires a single non-Kramers doublet with $g_\| \approx 8$ and $\delta \approx 0.3$ cm^{-1}, indicating that the ground state is $M_s = \pm 2$. Fits using $g_\| = 4$, 12, or 16 were poor (graphically and goodness of fit). An excited doublet at 1.9 cm^{-1} above the ground state with $g_\| \approx 4$ (i.e., $M_s = \pm 1$) is required in order to fit the higher-temperature saturation data. Fits with an excited-state energy above 3 cm^{-1} did not fall within the standard deviation of the data set. Inclusion of a third excited state does not have a significant effect on the fitting results. A good fit for the 9500 cm^{-1} band also gives a ground state of $M_s = \pm 2$ and an excited state of $M_s = \pm 1$ at 1.9 cm^{-1} above the ground state. The parameters obtained for both bands are very similar (consistent with both transitions arising from the same ground state) and are given in Table 1. Included for comparison are the results for *E. coli* R2,[38] which has CD/MCD spectra extremely similar to those of DF2t (vide infra) and Δ^9D,[14] which was well-modeled by the Zn crystal structure of DF1.[20] Note that *E. coli* R2 also has a ground state with $g_\| \approx 8$ corresponding to $M_s = \pm 2$, whereas Δ^9D has a MCD-silent ground-state sublevel with $g_\| \approx 0$ and an $M_s = \pm 4$ ($g_\| \approx 16$) 11 cm^{-1} above the ground state. Hence, initial examination indicates that the spin states of DF2 are more similar to the *E. coli* R2 than Δ^9D.

To define the exchange-coupling parameter (*J*) and ZFS parameter (*D*) values of this coupled binuclear system, a spin-Hamiltonian analysis was performed to correlate to the ground-state sublevels of DF2t in Table 1. Equation 2 gives the expression for the spin-Hamiltonian of a general biferrous system, which operates on the uncoupled basis set $|S_1,S_2,M_{s1},M_{s2}\rangle$, where the subscripts indicate the two ferrous centers:

$$H = -2J\hat{S}_1\cdot\hat{S}_2 + D_1(\hat{S}^2_{z1} - {}^1/_3S(S+1)) + E_1(\hat{S}^2_{x1} - \hat{S}^2_{y1}) + D_2(\hat{S}^2_{z2} - {}^1/_3S(S+1)) + E_2(\hat{S}^2_{x2} - \hat{S}^2_{y2}) + g_{z1}\beta H_z\hat{S}_{z1} + g_{x1}\beta H_x\hat{S}_{x1} + g_{y1}\beta H_y\hat{S}_{y1} + g_{z2}\beta H_z\hat{S}_{z2} + g_{x2}\beta H_x\hat{S}_{x2} + g_{y2}\beta H_y\hat{S}_{y2} \quad (2)$$

Here, *J* is the exchange coupling between the two irons, D_1, D_2, E_1, and E_2 are the axial and rhombic ZFS parameters, and *H* is the magnetic field. Zeeman terms ($g_{z1}\beta H_{z1}S_{z1}$ ... etc.) are also included, where the *g* value can be coupled to the ZFS parameters using ligand field theory as given in eqs 2a and 2b: λ is the Fe(II) ground-state spin−orbit coupling constant (∼100

$$D_{\mathrm{Fe^{2+}}} = \frac{-k^2\lambda}{4}(g_{x\mathrm{Fe^{2+}}} + g_{y\mathrm{Fe^{2+}}} - 2g_{z\mathrm{Fe^{2+}}}) \quad (2a)$$

---

(35) Stevens, P. J. *Annu. Rev. Phys. Chem.* **1974**, *25*, 201.
(36) Zhang, Y.; Gebhard, M. S.; Solomon, E. I. *J. Am. Chem. Soc.* **1991**, *113*, 5162−5175.
(37) Bennet, D. E.; Johnson, M. K. *Biophys. Acta* **1987**, *911*, 71−80.
(38) Pulver, S. C.; Tong, W. H.; Bollinger, J. M., Jr.; Stubbe, J.; Solomon, E. I. *J. Am. Chem. Soc.* **1995**, *117*, 12664−12678.

$$E_{\mathrm{Fe}^{2+}} = \frac{-k^2\lambda}{4}(g_{y\mathrm{Fe}^{2+}} - g_{x\mathrm{Fe}^{2+}}) \qquad (2b)$$

cm^{-1}), and k^2 is the Stevens orbital reduction factor, i.e., ($|k| < 1$), and accounts for the effects of covalency.

A high-spin ferrous ion has an $S = 2$ ground state with $M_s = 0, \pm1$, and ±2. This five-fold degeneracy will split due to ZFS. In an exchange-coupled system, the two ferrous ions can also interact through bridging ligands to give $S_{\mathrm{tot}} = |S_1 + S_2|$ ... $|S_1 - S_2| = 4, 3, 2, 1$, and 0 levels. These levels are split by the exchange coupling $H = -2JS_1{\cdot}S_2$ to generate $(2S_{\mathrm{tot}} + 1)M_s$ degenerate levels, which are further split in energy by ZFS. Since the magnitudes of D and J are comparable in binuclear non-heme ferrous systems, their combined effects need to be considered.

A 25 × 25 matrix describing the interaction of M_s sublevels with each other as functions of J and D is generated, and diagonalization of this matrix in zero magnetic field gives the wave functions of the binuclear ferrous spin states and their energies, which are dependent on the relative magnitudes and signs of the exchange coupling and the ZFS. The magnitudes of the D's are constrained to be less than $|15|$ cm^{-1} (the largest value observed in model systems and ligand field calculations); the maximum $|E/D|$ is $^1/_3$ by definition. From Table 1, DF2t has a ground state with $M_s = \pm2$ ($g = 8$) and a lowest excited state of $M_s = \pm1$ ($g = 4$). This situation occurs when two D's are of opposite signs and is consistent with the 5C,4C structure deduced from the CD/MCD analysis. Figure 3 gives a representative energy level diagram with $D_1 = +5$ cm^{-1} and $D_2 = -10$ cm^{-1}. The left side of the figure gives antiferromagnetic coupling ($J < 0$), which generates a ground state of (S_{tot}, $\pm M_s$) = (2, ±2), (1, ±1), or (0, ±0) as J becomes more negative.

In Figure 3, the ground state and first excited state for the J-value range of -2.0 to 0 cm^{-1} are highlighted in red. The black arrow indicates the location[38] of *E. coli* R2, while the green arrow shows the position of DF2t with the values of J and D given in the bottom half of Table 1. DF2t is shifted to the left of *E. coli* R2 (i.e., more antiferromagnetic) as the $M_s = \pm1$ excited state and the $M_s = \pm2$ ground state are closer in energy. This decrease in energy between the ground and excited states is due to J becoming more negative, until there is a ground-state crossover at $J = -2.0$ cm^{-1}. Thus, the binuclear site of DF2t is more antiferromagnetically coupled than *E. coli* R2 but has not crossed over to an $M_s = \pm1$ ground state.

In the above VTVH MCD analysis for DF2t, second-order Zeeman contributions have been incorporated via the inclusion of the empirical B-term in the MCD intensity expression (B_i in eq 1). These empirical float parameters are used to account for the field-induced mixing between sublevels of the ground state. The data can also be fit directly with the spin-Hamiltonian wave functions and the fact that the MCD intensity is proportional to the spin-expectation values of the single iron center being studied by MCD projected onto the dimer states. This complementary fitting approach uses the parameters D_1, E_1, D_2, E_2, and J, and the effective transition moment products M_{xy}, M_{xz}, and M_{yz}, to obtain the best fit. In this approach, D_1 is the Fe$^{\mathrm{II}}$ center associated with the d → d transition studied by VTVH MCD. Details of the simulation program are given in ref 12. The spin-Hamiltonian parameters derived from both methods are consistent with each other.

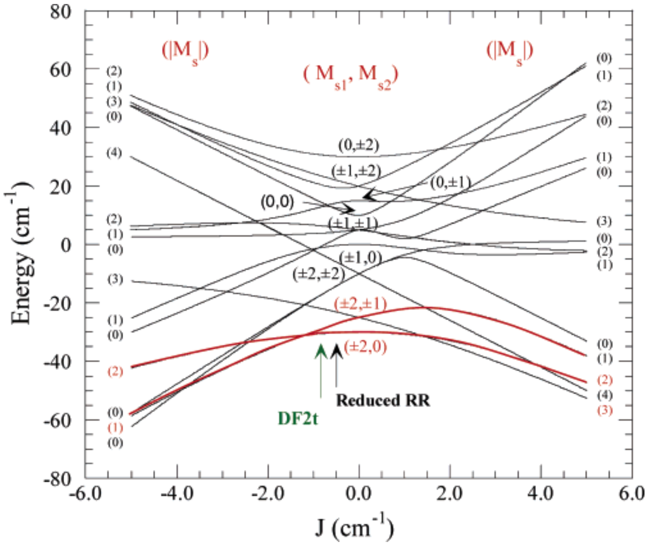

Figure 3. Correlation diagram of the energy levels of the binuclear ferrous ground state with $D_1 = +5$ cm^{-1} and $D_2 = -10$ cm^{-1}. The right side of the entire diagram indicates a ferromagnetic interaction ($J > 0$) between the ferrous atoms, and the left an antiferromagnetic interaction ($J < 0$). The ground state and first excited state for $-2.5 < J < 0.5$ cm^{-1} are outlined in red.

Initially, a variety of VTVH MCD simulations were performed to map out the solution space. The best fits to the VTVH MCD data are shown in Figure 4 and summarized in Table 2. A good fit to the VTVH MCD data in Figure 2 collected at 7500 cm^{-1} could be obtained only if this transition is associated with the Fe$^{\mathrm{II}}$ center with a positive ZFS. Figure 4A,B shows the fits using $D_1 = +5$ versus $D_1 = -10$. The fit for $D_1 = -10$ does not fall within the standard deviation of the data collected and can be eliminated. Thus, the spin-Hamiltonian analysis verified that the peak at 7500 cm^{-1} for DF2t is best fit with $D_1 = +5$ cm^{-1}, $D_2 = -10$ cm^{-1}, and $J \approx -0.8$ cm^{-1}. Consequently, the 7500 cm^{-1} saturation data can be correlated to the Fe$^{\mathrm{II}}$ with a positive ZFS which, from ligand field theory, should be the 4C iron. A fit to the 9500 cm^{-1} saturation data (Figure 4C,D) could be obtained with only a negative D value.[39] Thus, the MCD band at 9000 cm^{-1} is assigned to the 5C iron. This result is consistent with the B-term fitting method, giving confidence in our MCD peak assignments and description of the coordination number at each iron.

In summary, the reduced form of DF2t contains a 4C,5C diiron center, with the peaks at 8090 and 5450 cm^{-1} being associated with the 4C iron and the 9000 cm^{-1} transition associated with the 5C iron. The complex has a weak antiferromagnetic coupling J value of -0.8 cm^{-1}, indicating the presence of a μ-1,3 carboxylate bridge.

The spectroscopic similarity of DF2t to R2 and its closely related reactivity with oxygen (vide infra), along with recent studies of the peroxo intermediate in R2, have prompted us to examine the factors which affect the O$_2$ reactivity of these binuclear ferrous sites, in particular the formation of a bridged versus terminal bound O$_2$ intermediate.

---

(39) The (+) and (−) notation refers to relative phases of orbitals in the (x, y, z) molecular coordinate system. For the Fe-based orbitals, (+) also indicates gerade inversion symmetry, while (−) is ungerade. For the oxo-based orbitals, $p_y(-)$ corresponds to the σ-bonding orbital of molecular O$_2$, $p_y(+)$ is σ^*, $p_x(+)$ is the in-Fe2O2-plane π-orbital, $p_x(-)$ is π^*, $p_z(+)$ is the out-of-plane π-orbital, and $p_z(-)$ is π^*. This nomenclature does not imply an oxo−oxo overlap at r(O−O) = 2.499 Å.

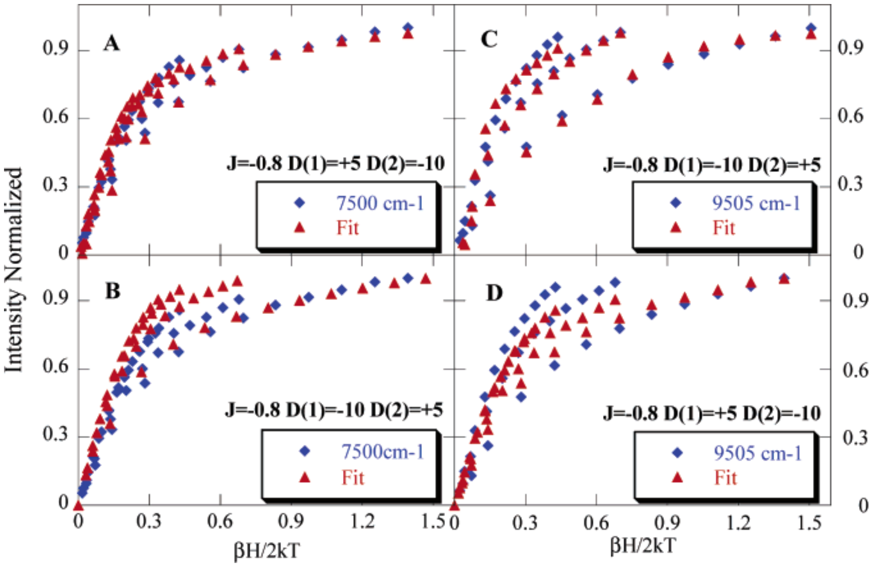

Figure 4. Fit of reduced DF2t using the complete spin-Hamilton. VTVH fit (red) is overlaid with the normalized VTVH data (blue) for (A) 7500 cm^{-1} with $D_1 = +5$, $D_2 = -10$; (B) 7500 cm^{-1} with $D_1 = -10$, $D_2 = +5$; (C) 9500 cm^{-1} with $D_1 = -10$, $D_2 = +5$; and (D) 9500 cm^{-1} with $D_1 = +5$, $D_2 = -10$.

Table 2. Spin-Hamiltonian Parameters for *E. coli* R2, DF2t, and Δ^9D without Substrate

	E. coli R2	DF2t		Δ^9D
	7700 cm^{-1}	7500 cm^{-1}	9500 cm^{-1}	7700 cm^{-1}
J (cm^{-1})	−0.44	−0.8	−0.8	<∼−1.0
D_1 (cm^{-1})	4	5	−10	$-15 < D < -5$
D_2 (cm^{-1})	−10	−10	5	$-15 < D < -5$

C. Density Functional Calculations. DFT calculations of the energetics of forming an end-on terminally bound O_2 were pursued in order to explore the first step in the reaction between a biferrous site and dioxygen. Given the close similarity between the crystallographically and spectroscopically determined active-site geometries of R2-D84E and DF2t, we used previous calculations of R2-D84E as a reference, in which the O_2-bridged structure has been calculated.[29] Here, the terminal mode of binding is evaluated in exactly the same manner to allow comparison between the two structures. These also parallel our past studies of O_2 binding to mononuclear non-heme Fe enzymes,[40] except there is the additional presence of carboxylate bridges to the second Fe in the binuclear system. The interactions resulting from the second sphere were accounted for in the present study by constraining the α-carbon positions of the coordinating residues and including models of the second coordination sphere residues that have large protein field interactions with the active site. Thus, the relative energetics of O_2 binding end-on to one Fe of the biferrous site versus bridging both irons can be evaluated in the same protein environment. These calculations use the well-defined computational active-site model of the R2 variant, R2-D84E,[41] as a reference system. This model was found to predict the coordination geometry of the biferrous state of R2-D84E and a μ-1,2 coordination geometry for its peroxo intermediate.[29] Both of these predictions correlate well with experimental data. The biferrous spectra of R2-D84E[16] are very similar to those of DF2t, suggesting that this well-defined computational model is appropriate for probing the energetics of terminal O_2 binding to biferrous non-heme iron sites.

The coordination geometry of the biferrous form of the R2 active site has been identified to be five-coordinate at Fe(1) (the iron coordinated to E84 of R2) and four-coordinate at Fe(2) (the iron coordinated to E204).[12,42] Although both irons are coordinatively unsaturated, Fe(2) is sterically most accessible. In DF2t, the two monomers in the dimers have the same sequence, although the overall complex is intrinsically asymmetric with one four-coordinate iron and one five-coordinate iron. By analogy to R2, we designate the four-coordinate site as Fe(2) and explore the binding of O_2 to this less hindered site.

There are multiple possible product spin states that can arise from combining dioxygen with the resting, antiferromagnetically coupled, biferrous site of R2. $S = 1$, the starting spin state of the system, and $S = 0$, the spin state observed for the biferric-peroxo intermediate, were explored computationally. Other spin states, such as those involving a ferromagnetically coupled, binuclear iron site, were not considered, as requiring additional spin changes during the oxygen activation reaction would slow enzyme kinetics considerably. A number of initial geometries were probed to define the potential energy surface for each spin state. Geometry optimizations with $S = 1$ resulted in O_2 being dissociated as triplet-O_2 and the binuclear iron site returning to the resting biferrous structure identified previously. This result was independent of the starting geometry used. The $S = 0$ starting geometries resulted in either a monodentate terminal Fe−O−O structure (Figure 5A) or the bridging μ-1,2 biferric-peroxo structure (Figure 5B), depending on the starting geometry chosen. The μ-1,2 biferric-peroxo species is the same as the experimentally observed W48F/D84E-R2 peroxo intermediate in ref 24. The factor that determined the final O_2 coordination geometry was the initial proximity of the non-coordinated oxygen atom of the O_2 moiety to Fe(1); if this separation was

---

(40) Schenk, G.; Pau, M. Y. M.; Solomon, E. I. *J. Am. Chem. Soc.* **2004**, *126*, 505−515.

(41) Baldwin, J.; Voegtli, W. C.; Khidekel, N.; Moenne-Loccoz, P.; Krebs, C.; Pereira, A. S.; Ley, B. A.; Huynh, B. H.; Loehr, T. M.; Riggs-Gelasco, P. J.; Rosenzweig, A. C.; Bollinger, J. M., Jr. *J. Am. Chem. Soc.* **2001**, *123*, 7017−7030.

(42) Pulver, S.; Froland, W. A.; Fox, B. G.; Lipscomb, J. D.; Solomon, E. I. *J. Am. Chem. Soc.* **1993**, *115*, 12409−12422.

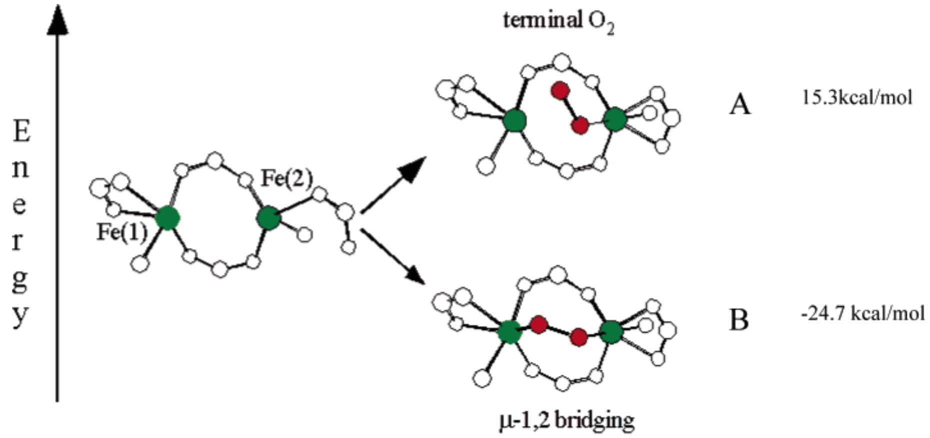

Figure 5. Structures identified from geometry optimization of the broken-symmetry $M_s = 0$ spin state. The resting structure on the left was reacted with oxygen in either an end-on fashion to one iron or bridging to both irons.

sufficiently short, the bridging biferric-peroxo shown in Figure 5B was formed. The energy of the terminal-O_2 species is 15.3 kcal/mol higher than that of the biferrous + O_2 starting species, and 40 kcal/mol higher than that of the μ-1,2 biferric-peroxo structure (Figure 5B).

The terminal-O_2 species is five-coordinate at Fe(1) and six-coordinate at the O_2-bound Fe(2) (Figure 6A). The Fe(2)−O(1) distance is slightly longer than the ferric-peroxo bond lengths (1.91 vs 1.88 Å), while the O−O distance (1.28 Å) is between those of peroxo (1.44 Å) and triplet-O_2 (1.21 Å). These bond lengths are strikingly similar to those calculated for the mononuclear ferric-superoxo species in ref 39: $r(\text{Fe}-\text{O}) = 1.88$ Å and $r(\text{O}-\text{O}) = 1.29$ Å. The remainder of the structure is similar to that obtained from prior biferrous and biferric-peroxo geometry optimizations.[16,29]

The orbital populations (Table 3) identify four unoccupied majority 3d orbitals on both Fe(1) and Fe(2) and two unoccupied majority O_2 orbitals, $\pi^*_\pi(\alpha)$ and $\pi^*_\sigma(\beta)$. The π^*_π orbital (α-spin) is 57% π^*_π but has 38% Fe(2) character, a large covalency, while the complementary occupied, majority Fe(2) $3d_{xz}$* orbital is 58% Fe(2) (and 30% π^*_π). The 38% Fe(2) character in π^*_π indicates that the O_2 ligand has accepted significant electron density from Fe(2). The four unoccupied Fe 3d β-spin−orbitals are located on Fe(1) (Table 3, bottom), while the LUMO is O_2 π^*_σ in nature (Figure 6B). The LUMO has contributions from both Fe(1) (11% xy) and Fe(2) (17% z^2), even though there is no bond between Fe(1) and the O_2 ligand. This charge transfer is facilitated by the bridging carboxylate ligands, which weakly couples the Fe(1) xy and O_2 π^*_σ orbitals. However, the primary iron contributor to this orbital is Fe(2), to which the O_2 moiety is directly bound.

The formal oxidation state of O_2 is reflected by the total amount of unoccupied $O_2(\pi^*)$ spin−orbital character. In the ionic limit, dioxygen has two, superoxide has one, and peroxide has no π^* spin−orbital character. For the bridged peroxo species in Figure 5B, the total unoccupied π^* spin−orbital character is 113% (Supporting Information B). The peroxo species has large electron donation to each of the two iron atoms (56% of an electron), due to the two strong donor bonds present in this structure. The calculated net π^* density in both the unoccupied α- and β-spin−orbitals of the end-on structure (O_2-bound only to Fe(2)) is 142%. This charge donation is higher than in the peroxo species and occurs with only one metal−ligand bond. This identifies the end-on structure as a mixed-valent Fe(II)-Fe(III) superoxide species with O_2^- bound to Fe^{III}. Although not directly comparable due to the different basis sets used, the net unoccupied π^* density of the mononuclear ferric-superoxo species calculated in ref 39 is 136%. The electronic structure of the terminal O_2-bound species is thus an $S = 2$ ferric-superoxo unit antiferromagnetically coupled to a high-spin distal ferrous $S = 2$ iron to form an $S = 0$ total spin state.

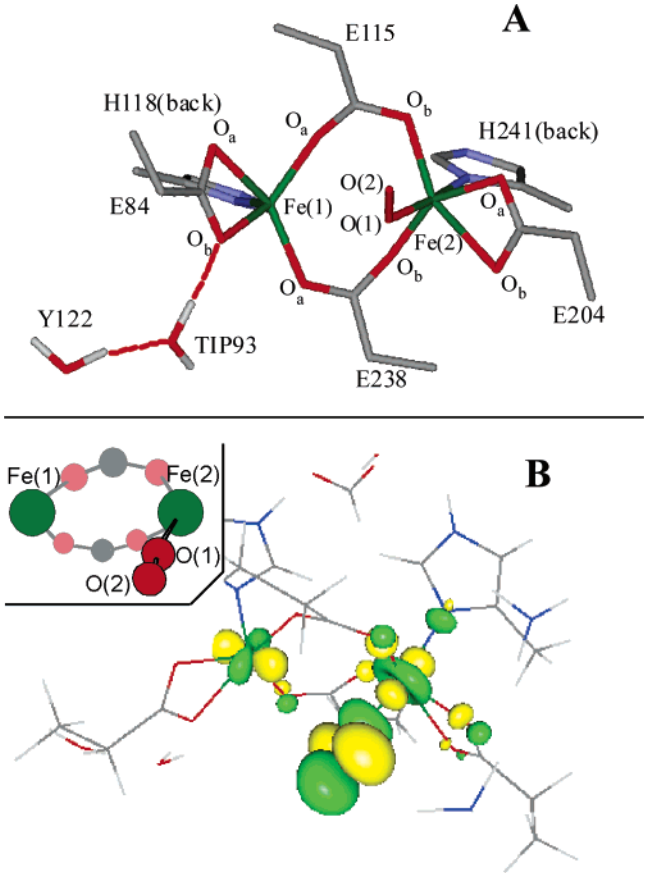

Figure 6. (A) Structure of the $S = 0$ terminal O_2 structure. Metrics of interest (bond lengths in angstroms, bond angles in degrees): $r(\text{Fe(1)}-\text{Fe(2)}) = 3.84$, $r(\text{O(1)}-\text{O(2)}) = 1.28$, $r(\text{Fe(2)}-\text{O(1)}) = 1.91$, $r(\text{Fe(1)}-\text{O(1)}) = 3.28$, $r(\text{Fe(1)}-\text{O(2)}) = 3.94$, $r(\text{Fe(2)}-\text{O}_{\text{a,E204}}) = 2.09$, $r(\text{Fe(2)}-\text{O}_{\text{b,E204}}) = 2.37$, $r(\text{Fe(2)}-\text{O}_{\text{b,E115}}) = 2.04$, $r(\text{Fe(2)}-\text{O}_{\text{b,E238}}) = 1.97$, $\angle(\text{Fe(2)}-\text{O(1)}-\text{O(2)}) = 122°$, $\angle(\text{Fe(1)}-\text{Fe(2)}-\text{O(1)}) = 58°$. Full coordinates are given in Supporting Information S4. (B) Isopotential surface of the β-spin LUMO orbital. Inset: cartoon of the structure orientation for reference.

Table 3. Compositions of the α-Spin (Top) and β-Spin (Bottom) O2 and Fe 3d-Derived MOs for the Terminal O2 Model Obtained from Spin-Unrestricted Broken Symmetry ($M_S = 0$) Calculations[a]

E (eV)		orb[b]	Fe1	O1	O2	O_2 orb	Fe2	E115	E238
−0.32		z^2	0	8	3	π^*_σ	69	3	6
−1.02		xy	0	0	0		77	6	5
−1.75		x^2-y^2	0	4	5	π^*_π	79	2	7
−1.83		π^*_π	0	27	30	π^*_π	38	1	1
−2.02	LUMO	yz	0	2	2		87	1	3
−3.24	HOMO	xz	0	7	23	π^*_π	58	1	1

E (eV)		orb[c]	Fe1	O1	O2	O_2 orb	Fe2	E115	E238
−0.24		x^2-y^2	77	0	0		0	2	6
−0.90		z^2	83	0	0		0	4	2
−1.33		xz	85	0	0		0	8	1
−1.53		yz	88	0	0		0	2	1
−2.17	LUMO	π^*_σ	11	27	34	π^*_σ	17	2	3
−2.48[d]		xy	81	5	6	π^*_σ	2	1	2

[a] The columns labeled "E115" and "E238" are the total orbital contribution from the CO2 tail of the glutamate R-group. The "remainder" in each row (i.e., rows not summing to 100%) is due to the contribution from the other ligands (H118, E84, ...) to the orbital. Note: O1 is the oxygen coordinated to Fe2 [b] Coordinate system (for Fe2): z = Fe2−O(1) bond vector, $x \approx$ bisects Fe2−$O_{a,E204}$ and Fe2−$O_{b,E204}$ bonds, $y \approx$ bisects Fe2−$O_{a,E204}$ and Fe2−$O_{b,E115}$ bonds. [c] Coordinate system (for Fe1): $z \approx$ Fe1−$O_{b,E84}$ bond vector, $x \approx$ Fe2−$O_{a,E84}$ bond, $y \approx$ Fe2−N_{H118} bond. [d] The HOMO consists of a ligand orbital with zero occupation.

Although the calculated energies of superoxo formation differ somewhat between the mononuclear[40] and binuclear cases, both are uphill and their structures are quite similar. The quantitative difference in energy between the two reactions is due to a combination of several factors. These include different basis set, different structural constraints due to the protein environment of the two models, and the inclusion of a solvent dielectric in the mononuclear calculation which is required for a model of the solvent-exposed 2,3-dihydroxybiphenyl 1,2-dioxygenase (DHBD) active site but unnecessary in the buried active site of R2. As noted above, the Fe−O and O−O distances are nearly the same. The Fe−O−O angle is more open in the mononuclear structure (130° vs 122°), while the average bond lengths of the remaining nitrogen and oxygen donors to the coordinating iron are slightly greater in the binuclear structure (2.16 Å vs 2.12 Å).[40] These limited differences are most likely due to the use of the LACVP* description for the iron in the binuclear optimization versus 6-311G* description in the mononuclear case. Previous mononuclear studies found that the geometry of the Fe−O−O unit is highly sensitive to the basis set used in the optimization.

Discussion

CD/MCD/VTVH MCD analyses of DF2t have determined that the reduced binuclear iron active site has one five-coordinate iron and one four-coordinate iron. The interaction between the two irons is weakly antiferromagnetic, indicating the presence of a poor superexchange pathway, consistent with μ-1,3 carboxylate bridging. The spectra of DF2t are remarkably similar to those of the active site of reduced *E. coli* R2[38] (Figure 7). Resting Δ^9D has also been included for comparison,[14] since the crystal structures of DF1 and DF2t complexed with divalent transition metal ions[20] resemble the resting Δ^9D.

Based on the known crystal structure of di-Zn(II) and di-Mn(II) derivatives of proteins in the DF2 family and the family of binuclear non-heme iron enzymes (R2, MMO, Δ^9D), the "default" structure of a biferrous site has two bridging carboxylates, two terminal potentially chelating Glu carboxylates, and two His ligands, giving a total of four or five ligands to each metal ion, depending on the coordination of the terminal and bridging carboxylates.[21] DFT calculations have found small energetic differences between a μ-1,1(η^1,η^2) and a μ-1,3 carboxylate bridge,[10,16,43] but spectroscopy can be used to differentiate the two in most cases, as the exchange-coupling parameter *J* depends on the orbital pathways, with the former displaying ferromagnetic coupling and the latter antiferromagnetic coupling.[16] In addition, one of the terminal glutamates can coordinate in a monodentate orientation, which would result in a (4C,5C) structure. The biferrous crystal structure of DF2t (complicated with an acetate from the crystallization buffer coordinated to one iron) indicates that it has a μ-1,3 carboxylate bridge and a 4C,5C binuclear site.[44]

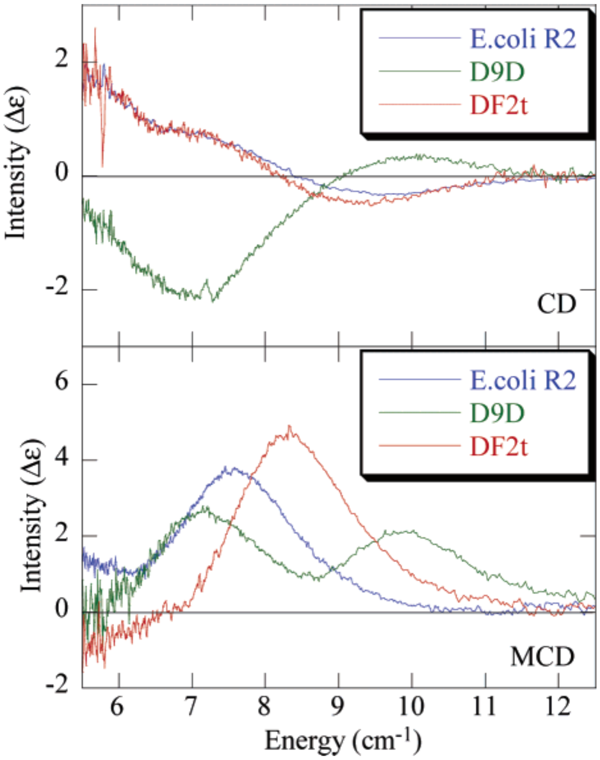

Figure 7. CD (top) and low-temperature MCD (bottom) spectra of *E. coli* R2 (blue), Δ^9D (green), and DF2t (red).

The rate of O_2 reactivity for DF2t has been measured to be ~25 min^{-1} (Supporting Information C).[45] From Table 4, this rate is on the same order as that for the reaction of *E. coli* R2 and its D84E variant with oxygen.[46] Alternatively, the rate of reaction of resting Δ^9D (without substrate) to O_2 is ~0.002 min^{-1}.[47] Upon binding of the substrate, acyl-ACP, the rate of reaction become comparable to that for R2.[48] This difference in O_2 reactivity correlates well to changes in spectral features,

---

(43) Torrent, M.; Musaev, D. G.; Morokuma, K. *J. Phys. Chem. B* **2001**, *105*, 322−327.
(44) Unpublished results.
(45) In the reaction of DF2t with oxygen, the ferric-oxo dimer state is the only species observed, suggesting that the reaction with dioxygen is rate-limiting and the decay of the peroxy intermediate is fast. The kinetics of the reaction of iron-loaded DF2t with dioxygen are described in Supporting Information C.
(46) Tong, W. H.; Chen, S.; Lloyd, S. G.; Edmondson, D. E.; Huynh, B. H.; Stubbe, J. *J. Am. Chem. Soc.* **1996**, *118*, 2107−2108.
(47) Cahoon, E. B.; Lindqvist, Y.; Schneider, G.; Shanklin, J. J. *Proc. Natl. Acad. Sci. U.S.A.* **1997**, *94*, 4872−4877.
(48) Broadwater, J. A.; Ai, J. Y.; Loehr, T. M.; Sanders-Loehr, J.; Fox, B. G. *Biochemistry* **1998**, *37*, 14664−14671.

Table 4. Rate of O_2 Reaction (min^{-1}) with the Fully Reduced Form of the Diiron Enzyme at 5C[5,15,45−48]

Δ^9D alone[a]	~0.002
MMOH alone[a,b]	~1.3
DF2t[a]	~25
Δ^9D-ACP[c]	~20−30
R2-W48F/D84E[c]	~138
R2 (*E. coli*)[d]	~60
MMOH + MMOB[b,e]	~1320

[a] Measured by the appearance of the μ-oxo charge transfer band at 350 nm. [b] Meaured by the reaction rate of the biferrous enzyme with O_2. [c] Measure by the formation of the peroxo-diferric intermediate. [d] Measured by the formation of intermediate X, as the decay of the peroxy intermediate is fast. [e] Addition of component B to MMOH increases the reactivity by 1000-fold.

as VTVH MCD shows that the 5C,5C Δ^9D site becomes 4C,5C upon substrate binding.[14] It is interesting to note that, although there is no coordination change in MMOH, a noticeable spectral and structural change occurs upon component B binding which correlates to an increase in its reactivity with O_2.[5,42]

DFT calculations have examined the correlation between structure and reactivity. When O_2 was allowed to react with a 5C,4C antiferromagnetically coupled biferrous site, the reaction course was determined by whether the second oxygen was allowed to react with the distal Fe^{II}. The only energy-minimized structures obtained from terminal-bound O_2 starting geometries were monodentate superoxo-[Fe(III)Fe(II)] and cis-μ-1,2 peroxo-biferric $[Fe(III)]_2$. Geometry optimization favored the cis-μ-1,2 peroxo-$[Fe^{III}]_2$ model over the terminal-O_2 species by 40 kcal/mol, with the latter being unfavorable relative to O_2 and the reduced site. In fact, to obtain the terminal structure, the second oxygen must be orientated to prevent it from reacting with the remote Fe. Structural optimization resulted in an Fe^{III}-superoxo species with high-spin Fe^{III} $S = {}^5/_2$ antiferromagnetically coupled to O_2^- $S = {}^1/_2$ (Figure 5 and Table 3). This significant energy difference (40 kcal/mol) is due to the energetically favored two-electron reduction of dioxygen to peroxide (based on the two- vs one-electron reduction potential of dioxygen: 390 vs −140 eV)[49,50] the ability of the peroxide to form strong donor bonds to each of the two Fe^{III} in the μ-1,2 bridged state, and as developed in ref 31, the fact that superoxide only weakly binds to high-spin Fe^{III}. Thus, a determinant of O_2 reactivity of carboxylate-bridged binuclear Fe^{II} sites appears to be whether O_2 can bridge both irons to form to a peroxo-biferric structure.

It is interesting to compare these results to those obtained with hemerythrin (Hr),[51] where triplet-O_2 binds to one iron in deoxyHr to form a terminally bound hydroperoxide.[52,53] The two irons are bridged by an OH, which becomes an oxo bridge along the reaction coordinate of O_2 binding. This provides a good superexchange pathway to allow a second electron to transfer from the remote iron to O_2. The O_2-activating enzymes and DF2t have only carboxylate bridges, which provide poor superexchange pathways in comparison to the oxo bridge. Biferrous structures that do not have an additional OH/oxo bridge would be suited for O_2-activation, as the peroxo-biferric structure would not be stabilized by the presence of an additional oxo bridge and thus activated for further oxidation with O−O cleavage.

This work has led to a deeper understanding of how the protein matrix can promote the formation of a reversible, end-on peroxo species in Hr versus oxygen consumption in catalytic diiron proteins. The presence of five neutral His ligands and only two negatively charged carboxylate ligands in Hr helps recruit a hydroxylate ion, which partially neutralizes the high overall positive charge on the biferrous center. The resulting μ-hydroxide bridge serves several roles: (1) it completes the coordination sphere of one of the two ferrous ions, thereby precluding a 1,2 bridging interaction; (2) it facilitates superexchange and two-electron reduction of O_2 to peroxo; and (3) the hydroxyl proton is available for transfer to the bound peroxide, further stabilizing the complex. By contrast, the presence of four Glu and two His ligands in a pseudo-two-fold symmetrical array in O_2-utilizing diiron proteins presents open coordination sites on both metal ions trans to the strong His ligands. The resulting complex is formally neutral and well-suited to bind O_2 in a bridging conformation with concomitant electron transfer to form a μ-1,2 peroxo-diferric complex and potentially subsequent ferryl species. Future studies of the de novo family are being pursued to understand how structural differences can affect the binuclear active site and contribute to dioxygen reactivity.

Acknowledgment. We acknowledge financial support by the NSF-Biophysics Program Grant MCB-0342807 (E.I.S.), NSF Chemistry CHE96343646 (W.F.D.), and NSF Pre-Doctoral Fellowship to P.-p.W.

Supporting Information Available: Overlay of the MCD of aqueous Fe(II) and reduced DF2t, the model cis-μ-1,2 spin-down Fe d-orbital compositions using the BP86 functional, the absorbance at 350 nm monitored as a function of time for the formation of the Fe(III) oxo-bridged DF2t, and the geometry-optimized end-on superoxo structure coordinates. This material is available free of charge via the Internet at http://pubs.acs.org.

JA053661A

---

(49) Marcus, M. A.; Sutin, N. *Biochim. Biophys. Acta* **1985**, *811*, 265−302.

(50) Bieliski, B.; Cabelli, D.; Arudi, R. L. *J. Phys. Chem. Ref. Data* **1985**, *14*, 1041−1100.

(51) Reem, R. C.; Solomon, E. I. *J. Am. Chem. Soc.* **1987**, *109*, 1216−1226.

(52) Brunold, T. C.; Solomon, E. I. *J. Inorg. Biochem.* **1999**, *74*, 85.

(53) Brunold, T. C.; Solomon, E. I. *J. Am. Chem. Soc.* **1999**, *121*, 8288−8295.